






## PAPER

[View Article Online](#)  
[View Journal](#) | [View Issue](#)Cite this: *J. Mater. Chem. A*, 2020, **8**, 14975

# Investigating the effect of a fluoroethylene carbonate additive on lithium deposition and the solid electrolyte interphase in lithium metal batteries using *in situ* NMR spectroscopy†

Anna B. Gunnarsdóttir, <sup>a</sup> Sundeep Vema, <sup>ab</sup> Svetlana Menkin, <sup>a</sup>  
Lauren E. Marbella <sup>‡a</sup> and Clare P. Grey <sup>\*a</sup>

Using lithium metal as the negative electrode in a rechargeable lithium battery can increase the energy density, but to date, its use is limited due to uncontrolled and inhomogeneous electrodeposition upon cycling, leading to both low coulombic efficiencies and safety issues. The solid electrolyte interphase (SEI) has been identified as a key component in controlling microstructural growth but its role is still not well-understood. Here we explore the effect that fluoroethylene carbonate (FEC), a common electrolyte additive, along with pulse plating, has on the SEI on lithium metal and the electrodeposition of lithium. *In situ* NMR techniques, which are both non-invasive and quantitative, are used to monitor the microstructural growth during lithium deposition. We show how lithium whisker growth in a commercial carbonate electrolyte leads to increased SEI formation and low current efficiency, whereas using an FEC additive leads to denser lithium metal electrodeposits. We use <sup>6,7</sup>Li isotopic labelling to monitor the exchange between lithium metal and the electrolyte and develop a numerical model to describe the process, which is discussed in the context of the standard model of electrochemical kinetics. The model allows us both to extract an exchange current density at the open circuit voltage, which takes into account the growth of the SEI and allows the extent of Li metal corrosion to be quantified. The results demonstrate that the isotope exchange rate depends significantly on the electrolyte and the corresponding SEI. The numerical simulations show that with an FEC additive the exchange is twice as fast as without, which is attributed to faster lithium ion transport in the SEI. Furthermore, the simulations indicate that FEC results in an accelerated SEI formation rate, more than four times faster than without the additive. These beneficial SEI properties, namely the fast lithium transport and faster SEI formation, help to explain why the fluorinated FEC additive results in a more uniform lithium deposition. The fast lithium ion transport will lead to a more homogeneous current distribution at the electrode surface. In the event that the SEI layer is ruptured, passivation of the freshly exposed lithium will occur more rapidly further leading to more homogeneous deposition.

Received 5th June 2020

Accepted 2nd July 2020

DOI: 10.1039/d0ta05652a

[rsc.li/materials-a](https://rsc.li/materials-a)

## Introduction

The search for higher energy density rechargeable lithium batteries has created a renewed interest in lithium (Li) metal anodes. Li metal has the highest volumetric and gravimetric energy density of all negative electrodes, however, it suffers from both capacity fading and safety issues.<sup>1,2</sup> The uneven

electrodeposition of Li on the metal anode results in high surface area microstructures that can ultimately lead to potentially hazardous situations such as cell short-circuiting and thermal runaway. The microstructures formed under Li deposition can exhibit a wide range of morphologies including needle, whisker, bush-like, mossy and fractal dendrites.<sup>3,4</sup> A detailed understanding of the parameters that dictate the different growth modes of microstructural Li is necessary to develop effective strategies to mitigate microstructural growth and to enable the use of Li metal anodes in batteries.

Generally, the morphology of metal electrodeposits is influenced by the current distribution over the electrode surface, which is affected by factors such as the geometry of the cell, the nature of the electrode's surface, the specific resistivity of the electrolyte solution, the activation overpotential and the

<sup>a</sup>Department of Chemistry, University of Cambridge, Lensfield Road, Cambridge, CB2 1EW, UK. E-mail: [cpg27@cam.ac.uk](mailto:cpg27@cam.ac.uk)

<sup>b</sup>The Faraday Institution, Quad One, Harwell Science and Innovation Campus, Didcot OX11 0RA, UK

† Electronic supplementary information (ESI) available. See DOI: 10.1039/d0ta05652a

‡ Present address: Department of Chemical Engineering, Columbia University, 500 W 120<sup>th</sup> St, New York, NY 10027, USA.

concentration overpotential.<sup>5</sup> Of these parameters, the surface of the Li metal electrode is particularly complex because of the solid-electrolyte interphase (SEI) that forms instantaneously when Li metal is immersed in an electrolyte due to the decomposition of the electrolyte and precipitation of the reduction products on the electrode surface. Also, 'pristine' Li metal is covered by a native SEI layer, composed mostly of lithium oxides, hydroxides and carbonates, which forms even under inert atmospheres (e.g. in a glovebox), from trace amounts of oxygen, nitrogen, water and a variety of organic solvents. The morphology of Li deposits and the cycling performance is highly dependent on the choice of electrolyte system where improved cycling efficiencies are generally attributed to a uniform and highly ionic conductive SEI layer.<sup>6–11</sup> Thus, the main approach to tackle inhomogeneous Li deposition has been the development of a suitable liquid electrolyte system, by controlling the type of solvents, salts, and additives, and by varying the salt concentrations, with the goal of manipulating the corresponding chemical composition of the SEI. A fundamental question to address, in order to systematically tackle microstructural growth, is how the nature of the SEI on Li metal affects the plating and stripping on Li metal. Here we study the effect of the common additive, fluoroethylene carbonate (FEC), which has been shown to improve the coulombic efficiency of Li deposition compared to the standard LP30 electrolyte.<sup>11–15</sup> Many studies have highlighted chemical differences in the nature of this SEI: X-ray photoelectron spectroscopy (XPS) studies have reported increased fluorine content in the SEI formed with FEC,<sup>16</sup> and a LiF-rich SEI.<sup>15</sup> Others have reported that a more ordered SEI is formed with FEC, which results in homogeneous lithium stripping.<sup>17,18</sup> The challenge now is to identify why these differences alter the deposition and stripping performance, motivating further fundamental studies.

Electrochemical models based on the concentration gradients developed in the electrolyte have been established to describe fractal dendritic growth during Li electrodeposition.<sup>19–22</sup> Two different current regimes are predicted where the limiting current density,  $j_{\text{lim}}$ , is defined as:  $j_{\text{lim}} = \frac{2eC_0D}{t_aL}$  where  $e$  is the elementary charge,  $C_0$  is the initial electrolyte concentration,  $D$  is the ambipolar diffusion coefficient,  $t_a$  is the transport number for the anion in the electrolyte and  $L$  is the distance between the two electrodes.<sup>22</sup> In the high-current regime, for a current density  $j > j_{\text{lim}}$ , diffusion limitation leads to fractal dendritic growth at a characteristic time known as the Sand's time (the time at which the concentration of the anions drops to zero at the electrode surface under the influence of an applied potential).<sup>20–22</sup> The onset of dendrite growth for Li metal has been shown experimentally to correlate well with this theory.<sup>23,24</sup> Below  $j_{\text{lim}}$ , according to this theory, the concentration gradient in the electrolyte will reach a steady-state with a non-zero concentration of the ions at the electrode and dendrite growth *via* this mechanism is not expected.<sup>15,16</sup> However, irregular microstructural growth occurs in most cases, which has been associated with local inhomogeneities on the Li metal surface or in the SEI where preferential deposition sites

result in so-called "hot spots" with high local current density.<sup>3,6,23,25,26</sup> These preferential deposition sites can originate from inhomogeneous transport properties in the SEI or cracks in the SEI, where Li grows through the protrusions caused by internal stresses beneath the SEI, giving rise to mossy and/or whisker-like structures.<sup>27–30</sup>

The morphology and plating behaviour of Li metal is commonly studied with techniques such as scanning electron microscopy (SEM),<sup>31</sup> *operando* optical microscopy,<sup>22,32,33</sup> transmission electron microscopy (TEM)<sup>28</sup> and cryo-TEM.<sup>17,34</sup> Recently, a new analytic method, titration gas chromatography (TGG), was used to quantify *ex situ* the amount of inactive Li formed when plating and stripping Li on a copper current collector.<sup>35</sup> Electron paramagnetic resonance (EPR) has been demonstrated as a semi-quantitative and non-invasive technique to observe *operando* Li microstructural growth in a flooded cell.<sup>36</sup> Of these techniques, *in situ* nuclear magnetic resonance (NMR) and magnetic resonance imaging (MRI) are unique as non-invasive techniques that can also provide quantitative and temporal information on Li metal deposition. *Operando* NMR has been used to study Li and Na plating and stripping by continuously acquiring NMR spectra during an electrochemical measurement.<sup>23,37–43</sup> Bhattacharyya *et al.* developed a method to quantify and distinguish between different types of microstructures that form during Li deposition based on the skin depth effect of conductors and the bulk magnetic susceptibility (BMS) of Li metal in a magnetic field.<sup>37</sup> As electromagnetic waves penetrate metals to a certain depth called the skin depth, NMR is sensitive to the total surface area of the Li electrode.<sup>37,44</sup> The increase in signal intensity upon cycling can thus be attributed to the formation of high surface area structures. Furthermore, the resonance of microstructural Li can be distinguished from the bulk Li metal due to shifts caused by BMS effects.<sup>44</sup> Note that *operando* and *in situ* are often used interchangeably, the former referring to measurements made while the device is operating while the latter is more general and refers to measurements made of the intact device.

In this paper, we use *in situ* NMR to study the differences in plating behaviour and transport properties of the SEI in two electrolyte systems; the standard carbonate electrolyte 1 M LiPF<sub>6</sub> in ethylene carbonate and dimethyl carbonate (EC : DMC 1 : 1 v/v, referred to as LP30) and the same electrolyte with the FEC additive (LP30 + FEC). Symmetrical Li–Li cells were operated below  $j_{\text{lim}}$  where fractal dendritic growth is not expected, in order to study the mossy and microstructural growth of Li. We show that under constant current, a compact layer of microstructures form on the electrode surface in LP30 + FEC with high current efficiency compared to a more open whisker-like growth for LP30. In addition, experiments were performed using pulse electrolysis, an electrochemical method that has been used to deposit a range of metals where the advantages cited in the literature include improved control over the size of the metal deposits and less porous morphology.<sup>45–49</sup> Previous studies on Li pulse plating have both demonstrated a smoother morphology and a less porous microstructural layer on the Li electrode.<sup>31,50–53</sup> However, in order to study the effectiveness of Li pulse plating it is crucial to use a quantitative technique such as *in situ* NMR spectroscopy.



Finally, we use  ${}^6,{}^7\text{Li}$  isotopic labelling to monitor the exchange between the bulk Li metal and the electrolyte with NMR. Previously, isotopic labelling has been used to study the solid/liquid interface in heterogeneous systems including solids such as ion exchanger beads and ionic crystals.<sup>54–57</sup> Iltott and Jerschow used isotope exchange NMR measurements between an enriched  ${}^6\text{Li}$  metal and a natural abundance  ${}^7\text{Li}$  electrolyte to study the kinetics at the Li metal-electrolyte interface.<sup>58</sup> Here we use this method to study how the nature of the SEI in the two electrolytes under study affects the rate of isotope exchange. A numerical model of the isotope exchange between the lithium metal and electrolyte was developed based on the work of Huang and Tsai on isotope exchange in heterogeneous systems.<sup>57</sup> The exchange current, as described by Butler–Volmer theory, was used to capture the exchange flux at equilibrium.<sup>59</sup> The model describes a  ${}^6\text{Li}$ -enriched Li metal electrode, soaked in a natural abundance lithium electrolyte and is thus comparable to a lithium metal anode at an open circuit voltage (OCV). From the numerical simulations we estimate the rates of exchange and SEI formation, and from that identify the key beneficial effects of the FEC additive: faster  $\text{Li}^+$  transport through the SEI and faster SEI formation.

## Experiment and theory

### Experimental

**Materials.** The electrolyte used was 1 M  $\text{LiPF}_6$  in 1 : 1 v/v ethylene carbonate/dimethyl carbonate (EC/DMC; Sigma Aldrich, LP30). For experiments using an additive, fluoroethylene carbonate (FEC; Sigma Aldrich, 99%) was added to the electrolyte in 1 : 10 ratio by volume (LP30 + FEC). The water content of the LP30 electrolyte was measured with Karl Fischer titration and was <40 ppm. For *in situ* NMR experiments, Li electrodes were prepared by cutting fresh Li from a Li rod (Sigma, 99.9% trace metal basis, 12.7 mm diameter) and rolled with an Al roller inside a plastic bag (polyester pouch, VWR) to an approximate thickness of 0.15 mm. This ensures that the native SEI layer is minimal when the Li metal is immersed in the electrolyte. Similarly, the  ${}^6\text{Li}$  metal (Cambridge Isotope Laboratories, 95%  ${}^6\text{Li}$ ) supplied in mineral oil was rinsed with hexane (Sigma Aldrich) and rolled with an Al roller inside a plastic bag. In all coin cells, pre-cut lithium metal disks (LTS research, 99.95%) were used. The materials were stored and handled in an Ar atmosphere glovebox ( $\text{O}_2$ ,  $\text{H}_2\text{O}$  < 1 ppm, MBraun).

**Cell fabrication.** All cell assembly and disassembly was performed in an Ar atmosphere glovebox ( $\text{O}_2$ ,  $\text{H}_2\text{O}$  < 1 ppm, MBraun). The design and assembly of the *in situ* capsule cell (made from polyether ether ketone, PEEK) has been described before.<sup>60</sup> The capsule cell provides a constant pressure across the cell and a similar pressure for all the experiments, which gives an increased reproducibility between *in situ* experiments compared to earlier work on plastic bag-cells.<sup>44</sup> The Li rod was rolled as described above and cut into a rectangular electrode with a razorblade, dimensions around 4 mm  $\times$  13 mm. Two separators were used between the Li electrodes, both a glass microfiber separator (Whatman, thickness = 0.68 mm) and a polypropylene–polyethylene separator (Celgard 3501). The glass separator is used to reduce BMS effects inside the NMR

magnet by increasing the distance between the electrodes<sup>35</sup> and the polymer separator makes it possible remove the electrodes gently from the separator to study the Li morphology *ex situ*. The electrolyte consisted of 75  $\mu\text{L}$  of either LP30 or LP30 + FEC. Stainless-steel 2032 type coin cells (Cambridge Energy Solutions) with a conical spring and two 0.5 mm thick spacer disks were assembled with the pre-cut Li disks described above, glass microfiber separator (Whatman) and 75  $\mu\text{L}$  of either LP30 or LP30 + FEC. For isotope exchange NMR measurements, the  ${}^6\text{Li}$  metal was cut into a rectangular electrode with a razorblade, of dimensions 3 mm  $\times$  13 mm. The electrode was placed in an airtight 5 mm J-Young NMR tube filled with 400  $\mu\text{L}$  of electrolyte, LP30 or LP30 + FEC, and transferred as quickly as possible to the NMR spectrometer for the measurement, which took approximately 10 minutes.

**Electrochemical measurements.** Electrochemical measurements were performed using a Biologic VSP potentiostat with EC-Laboratory software. For symmetrical Li–Li *in situ* cells, galvanostatic constant current or pulsed current was applied in a single direction. For the *in situ* cell setup in this study, the calculated limiting current density,  $j_{\text{lim}}$ , is  $\sim 7 \text{ mA cm}^{-2}$  and all the cells are operating in the low current regime,<sup>23</sup> with the applied current densities 0.5–2  $\text{mA cm}^{-2}$ . For symmetrical Li–Li coin cells, the cells were pre-conditioned for 5 cycles using 0.02  $\text{mA cm}^{-2}$  for a total capacity of 0.04  $\text{mA h cm}^{-2}$  followed by 10 cycles using 0.5, 1 or 2  $\text{mA cm}^{-2}$  for 2  $\text{mA h cm}^{-2}$ . For impedance measurements, symmetrical Li–Li coin cells were pre-conditioned using 1  $\text{mA cm}^{-2}$  for 0.04  $\text{mA h cm}^{-2}$  for one cycle, followed by potentiostatic electrochemical impedance spectroscopy (EIS) measurements using 10 mV voltage perturbation at the open circuit voltage in a frequency range of 1 MHz to 1 Hz with 10 steps per decade. EIS measurements were performed every hour for the first 30 hours after cell assembly followed by less frequent measurements.

**NMR.** *In situ* NMR measurements were performed on a Bruker Avance 7.1 T spectrometer, operating at a Larmor frequency of 300.1 MHz for  ${}^1\text{H}$  and 116.6 MHz for  ${}^7\text{Li}$ . The spectra were recorded on a Bruker HX double resonance static probe with a solenoidal coil. The *in situ* capsule cell (described above) was aligned in a Ag solenoid coil such that the Li electrodes were oriented perpendicular to  $B_0$  and parallel with respect to the  $B_1$  rf field. For each cell, a series of single pulse experiments were recorded continuously during the entire length of the electrochemical measurement. For  ${}^7\text{Li}$  metal measurements, the pulse duration was chosen to give maximum intensity of the bulk Li metal (corresponding to a flip angle of  $133^\circ$  and 10.2  $\mu\text{s}$ ), a recycle delay of 1 s ( $T_1$  of  ${}^7\text{Li}$  metal  $\sim 100 \text{ ms}$ ) and 256 transients recorded. This resulted in an experimental time of  $\sim 4.5 \text{ min}$ . The  ${}^7\text{Li}$  signals were referenced to 1 M aqueous solution of LiCl at 0 ppm. The spectra were processed in Bruker Topspin software, using the automatic phase and baseline correction. Data processing was performed in *R*, with deconvolution of the peaks performed with home-built least-square fitting function described in more detail in the ESI†<sup>61</sup> and the data analysis was done using both dplyr and ggplot packages.<sup>62</sup> The theory developed by Bhattacharyya *et al.* was used to quantify the NMR signal of the Li metal and is



described in more detail in the ESI.<sup>†</sup><sup>37</sup> The skin depth in the Li metal in this study is  $d = 12.1 \mu\text{m}$  (see eqn S(2)<sup>†</sup>). All *in situ* measurements were performed at room temperature (293 K).

The  $^6\text{Li}$  NMR isotope exchange measurements were performed on a Bruker Avance III 300 spectrometer, operating at a Larmor frequency of 300.1 MHz for  $^1\text{H}$  and 116.6 MHz for  $^7\text{Li}$ . The measurements were recorded with a MicWB40 probe inside a Micro2.5 triple axis gradient system at 298 K, using a water-cooling unit, and using a 10 mm  $^1\text{H}$ - $^{19}\text{F}/^7\text{Li}$  coil.  $^7\text{Li}$  shifts were referenced to a 1 M aqueous solution of LiCl at 0 ppm. The electrode was centred in the NMR coil, with the Li metal placed perpendicular to the  $B_0$  field and parallel to the  $B_1$  radio-frequency (rf) field to get maximum excitation.<sup>63</sup> Single pulse experiments were recorded on a series of  $^7\text{Li}$  spectra. The recycle delay of 15 s and 48 transients in the  $^7\text{Li}$  NMR resulted in an experimental time of  $\sim 12$  min per spectrum. The recycle delay was chosen to ensure full relaxation of the electrolyte components, with the delay  $> 5 \times T_1$ .

Pulsed-field gradient (PFG) NMR was performed using the same MicWB40 probe at 298 K. A stimulated echo (STE) pulse sequence was used with a gradient pulse length of 2.5 ms, diffusion time of 200 ms, recycle delay of 3 s, number of transients 32, and by varying the gradient in 16 steps ( $3.2$ – $146 \text{ G cm}^{-1}$ ). The data was fit to the Stejskal–Tanner equation using Bruker Topspin Software.<sup>64</sup> The gradient strength was calibrated by measuring the  $\text{Li}^+$  diffusion coefficient of 0.25 M LiCl in water at 298 K, with the diffusion coefficient set to  $0.96 \times 10^{-9} \text{ m}^2 \text{ s}^{-1}$ .<sup>65</sup>

**Scanning electron microscopy (SEM).** After electrochemically plating, the *in situ* cells were transferred into an Ar glovebox, disassembled and mounted onto the SEM stage of the transfer module (Kammrath & Weiss, type CT0) and dried under vacuum. The electrodes were not rinsed with a solvent unless stated specifically. The samples were transferred into the SEM chamber using the air-sensitive transfer module under an inert atmosphere (Ar), without being exposed to air. SEM images were acquired with a Tescan MIRA3 FEG-SEM instrument at an acceleration voltage of 5.0 kV.

## Theory

**Numerical model of isotope exchange.** For a one-electron, one-step process at equilibrium, continuous oxidation and reduction takes place at the electrode/electrolyte interface. In the system under study where Li metal is soaked in an electrolyte and no overpotential applied, the equilibrium process is:



where the forward and backwards reactions occur at the same rate resulting in a zero net overall current, termed the exchange current density  $j_0$ .<sup>59</sup> The traditional exchange current density,  $j_0$ , describes the electron transfer kinetics of the electrochemical system. When described in terms of the Butler–Volmer formulation for  $\text{Li}^+/\text{Li}^0$  it is:<sup>59</sup>

$$j_0 = Fk_0[\text{Li}^+]^\alpha[\text{Li}^0]^{1-\alpha} \quad (2)$$

where  $F$  is the Faraday constant,  $k_0$  is the standard rate constant and  $\alpha$  is the transfer coefficient. The transfer coefficient is a constant (between 0 and 1) that reflects how closely the activated state resembles the oxidised or reduced products.<sup>66</sup> Boyle *et al.* showed how Li metal deposition is more accurately described by a Marcus-based model where the transfer coefficient  $\alpha$  is a function of the applied potential.<sup>67</sup> However, at small overpotentials (or at the OCV) the Butler–Volmer and Marcus-based theories should be indistinguishable.<sup>67</sup>

Eqn (2) can be rewritten in terms of the exchange flux at the interface  $J_0$  [ $\text{mol m}^{-2} \text{ s}^{-1}$ ], where  $j_0 = FJ_0$ . This equilibrium process (strictly the OCV process) can be followed *via* the isotope exchange current when an enriched Li metal electrode is soaked in a non-enriched electrolyte (for example), because the  $^6\text{Li}$  concentrations are not in equilibrium (*i.e.* the concentrations of  $^6\text{Li}$  are different in the Li metal and electrolyte). In contrast to the traditional model of current density  $j_0$  described in eqn (2), the rate of exchange determined in the current measurement will depend not only on the electron transfer kinetics of  $\text{Li}^+/\text{Li}^0$  but as well on the rate of the subsequent transport of the  $\text{Li}^+$  through the SEI. To make a distinction between our model and the traditional one, and to generalise our model, we will hereafter refer to the isotope exchange flux occurring at OCV measured here as  $J_{\text{ex}}$  [ $\text{mol m}^{-2} \text{ s}^{-1}$ ]; furthermore, since the SEI growth is continuous,  $J_{\text{ex}}$ , is expected to be time dependent (as explored below *via* two different models). The implications of these models within the standard Butler–Volmer formulation are discussed later.

To model the isotope exchange intensity curves measured we need to consider the concentration of  $^7\text{Li}$  in the metal,  $c_{\text{m}7}$ , at distance  $x$  from the SEI-metal interface and at time  $t$ , described in the following equation:

$$c_{\text{m}7}(x, t) = [\text{Li}^0]f_{\text{m}7}(x, t) \quad (3)$$

where  $f_{\text{m}7}(x, t)$  is the  $^7\text{Li}$  mole fraction at position  $x$  in the metal. The metal is of thickness  $2L$  (Fig. 1a) and is represented on a discretised one-dimensional grid, where  $x = 0$  represents the surface of the Li metal and  $x = L$  represents the centre of the metal. The concentration of Li in the metal electrode is  $[\text{Li}^0] = \frac{\rho}{M} = \frac{0.534 \text{ g cm}^{-3}}{6.94 \text{ g mol}^{-1}} = 77M$  where  $\rho$  is the density of lithium metal and  $M$  the molar mass. The initial condition for the fraction of  $^7\text{Li}$  in the metal is  $f_{\text{m}7}(x, 0) = 0.05$ , since we use a 95% enriched  $^6\text{Li}$  metal. Note that at time  $t = 0$  in the simulations, approximately 10 minutes have passed since immersing the enriched Li metal in the electrolyte and the start of the NMR experiment. This will only result in a minimal error in the initial starting condition as the experiment is performed over multiple hours and the second data point in the experimental measurements (at  $t \sim 25$  min) shows minimal change from the first data point ( $t = 0$  min) in mole fraction of  $^7\text{Li}$  in both electrolyte and metal. To test for this, the initial conditions of the first few points of  $f_{\text{m}7}(x, 0)$  were increased to 0.055, which qualitatively did not result in any significant changes between the fitted parameters between the two electrolytes.







**Fig. 1** A schematic showing (a) the geometry of the Li metal electrode, (b) Model I, which uses one fitting parameter, the isotope exchange flux,  $J_{\text{ex}}$  [ $\text{mol m}^{-2} \text{s}^{-1}$ ] to describe the isotope exchange and (c) Model II, which describes both isotope exchange and SEI formation, via  $J_{\text{ex}}(t)$  [ $\text{mol m}^{-2} \text{s}^{-1}$ ] that depends on the initial isotope exchange rate flux  $J_{\text{ex},0}$  and the SEI permeability constant  $\beta_{\text{ex}}$ . The relevant equations and equation numbers describing the processes are indicated in the schematics.

The concentration of  $^7\text{Li}$  electrolyte as a function of time is,  $c_{e7}(t) = [\text{Li}^+]f_{e7}(t)$  with the initial condition for the fraction of  $^7\text{Li}$  in the electrolyte,  $f_{e7}(0) = 0.92$  (the natural abundance of  $^7\text{Li}$ ). Since the diffusion coefficient in lithium metal,  $D_m$ , is more than four orders of magnitude smaller than the diffusion  $\text{Li}^+$  coefficient in the electrolyte (Table 1), the diffusion of  $\text{Li}^+$  throughout the electrolyte is considered instantaneous.

The self-diffusion of Li atoms within the metal is described by Fick's law:

$$\frac{\partial c_{m7}(x,t)}{\partial t} = D_m \frac{\partial^2 c_{m7}(x,t)}{\partial x^2}, \quad 0 < x < L \quad (4)$$

and the symmetric boundary condition at  $x = L$  is:

$$\frac{\partial c_{m7}(x=L,t)}{\partial x} = 0 \quad (5)$$

Due to the difference in isotope ratio between the electrolyte and metal, the flux at equilibrium  $J_{\text{ex}}$ , will lead to change in the isotope ratio of the metal and the electrolyte:

$$D_m \frac{\partial c_{m7}(x=0,t)}{\partial x} = J_{\text{ex}}(f_{e7}(t) - f_{m7}(0,t)) \quad (6)$$

The partial differential equations of the concentration of  $^7\text{Li}$  in the metal are coupled to the ordinary differential equation that describes the concentration of  $^7\text{Li}$  in the electrolyte, described as follows:

$$\frac{dc_{e7}(t)}{dt} = -\frac{S_a}{V_e} J_{\text{ex}}(f_{e7}(t) - f_{m7}(0,t)) \quad (7)$$

where  $S_a$  is the surface area of the soaked electrode and  $V_e$  is the volume of electrolyte.

**Model I** assumes that the SEI of Li metal is of fixed thickness and fits the experimental curves with one fitting parameter  $J_{\text{ex}}$  and eqn (3)–(7), as shown schematically in Fig. 1b.

**Model II** It was necessary to extend the model to take into account the temporal evolution of the SEI. In the system under study, where the SEI forms without any applied current, simultaneous oxidation of the Li metal to  $\text{Li}^+$  is required in order to maintain charge balance. This is illustrated here by one

**Table 1** List of all the model input parameters and methods used to measure or estimate their values

Symbol	Description	Value/unit	Determination
$S_a$	Surface area of Li metal	$8.2 \times 10^{-5} \text{ m}^2$	Measured
$L$	Half thickness of the Li metal	$0.12 \times 10^{-3} \text{ m}$	Estimated from $S_a$ and weight of Li metal
$V_e$	Volume of the electrolyte	400 $\mu\text{L}$	Measured
$D_m$	Self-diffusion coefficient in Li metal	$7.11 \times 10^{-15} \text{ m}^2 \text{ s}^{-1}$	Measured by NMR relaxometry at 298 K (in ref. 68)
$D_{\text{LP30}}$	Diffusion coefficient in LP30	$1.70 \times 10^{-10} \text{ m}^2 \text{ s}^{-1}$	Measured by PFG-NMR
$D_{\text{LP30+FEC}}$	Diffusion coefficient in LP30 + FEC	$1.74 \times 10^{-10} \text{ m}^2 \text{ s}^{-1}$	Measured by PFG-NMR
$[\text{Li}^+]_{\text{LP30}}$	Concentration of LP30 electrolyte	1000 $\text{mol m}^{-3}$	From supplier
$[\text{Li}^+]_{\text{LP30+FEC}}$	Concentration of LP30 + FEC electrolyte	909 $\text{mol m}^{-3}$	Diluted with 1 : 10 ratio of FEC



typical SEI reduction reaction, involving the ring-opening of the EC solvent molecule,<sup>69</sup> as follows:



When taken together, the overall reaction corresponds to:



Other SEI reduction reactions similarly consume  $\text{Li}_{\text{metal}}^0$  rather than  $\text{Li}^+$ . SEI formation has previously been modelled as being proportional to the exchange current density at the metal/electrolyte interface.<sup>70</sup> A similar approach is used here where the SEI formation,  $\text{d}N_{\text{SEI}}/\text{d}t$ , is taken to be proportional to  $J_{\text{ex}}$ :

$$\frac{\text{d}N_{\text{SEI}}}{\text{d}t} = \alpha_{\text{SEI}}(t)J_{\text{ex}} \quad (9)$$

where  $N_{\text{SEI}}$  [ $\text{mol m}^{-2}$ ] is the total number of moles of Li atoms participating in the SEI per surface area of Li metal and  $\alpha_{\text{SEI}}(t)$  is the SEI formation constant, a proportionality constant that captures the rate of the SEI formation. The isotope ratio of SEI that forms at each time step is assumed to be equal to the electrolyte,  $c_{\text{e}7}(t)$ . The SEI formation is expected to slow down with time and the formation constant  $\alpha_{\text{SEI}}(t)$  includes an exponential decay term that varies with the amount of SEI formed:<sup>71</sup>

$$\alpha_{\text{SEI}}(t) = \alpha_{\text{SEI},0} \exp(-\beta_{\text{SEI}}N_{\text{SEI}}(t)) \quad (10)$$

where  $\beta_{\text{SEI}}$  [ $\text{m}^2 \text{mol}^{-1}$ ] is the SEI growth constant. The growth of the SEI will also affect the overall permeability of the SEI and slow down the exchange flux over time, again captured with a decaying exponential:<sup>58</sup>

$$J_{\text{ex}}(t) = J_{\text{ex},0} \exp(-\beta_{\text{ex}}N_{\text{SEI}}(t)) \quad (11)$$

where  $\beta_{\text{ex}}$  [ $\text{m}^2 \text{mol}^{-1}$ ] is the SEI permeability constant.

In addition, the SEI formation will affect the isotope ratio in the electrolyte. According to eqn (8), the overall  $\text{Li}^+$  ion concentration in the electrolyte should remain constant, however, differences in isotope ratio between the electrolyte and metal will result in changes to the isotope concentration in the electrolyte,  $c_{\text{e}7}$ . Since the consumption of  ${}^7\text{Li}^+$  in the electrolyte to form the SEI is  $\frac{\text{d}N_{\text{SEI}}}{\text{d}t}f_{\text{e}7}(t)$  and the rate of  ${}^7\text{Li}^0$  metal oxidised to  $\text{Li}^+$  is  $\frac{\text{d}N_{\text{SEI}}}{\text{d}t}f_{\text{m}7}(0, t)$ , the change in moles of the  ${}^7\text{Li}$  isotope in the electrolyte as a result of the SEI formation is  $\frac{\text{d}N_{\text{SEI}}}{\text{d}t}(f_{\text{e}7}(t) - f_{\text{m}7}(0, t))S_{\text{a}}$ , and eqn (7) becomes:

$$\frac{\text{d}c_{\text{e}7}}{\text{d}t} = -\frac{S_{\text{a}}}{V_{\text{e}}} \left( J_{\text{ex}} + \frac{\text{d}N_{\text{SEI}}}{\text{d}t} \right) (f_{\text{e}7}(t) - f_{\text{m}7}(0, t)) \quad (12)$$

The final model, termed Model II and shown schematically in Fig. 1c, solves eqn (3)–(6) and (9)–(12) with the four fitting parameters,  $J_{\text{ex},0}$ ,  $\alpha_{\text{SEI},0}$ ,  $\beta_{\text{ex}}$  and  $\beta_{\text{SEI}}$ .

To use the models to fit the experimental data, the equations for Model I and II were discretised using the method of lines and solved using an ode-solver in MATLAB (ode45 function).<sup>72</sup> A nonlinear least-square solver (lsqcurvefit function) was used to fit the experimental data, the  ${}^7\text{Li}$  intensity of the metal and the  ${}^7\text{Li}$  diamagnetic intensity (including electrolyte and SEI), to the numerical model. The nlparci function was used to generate a 90% confidence interval of the fitting parameters. The skin depth of the Li metal is taken into account when fitting the model to the NMR intensity of the metal peak, the NMR being only sensitive to the surface of the Li metal (see eqn S(2) in the ESI†).

Note, the exact chemical composition of the SEI is unknown and thus the thickness of the SEI in both electrolytes,  $s(t)$ , can only be compared by assuming a chemical composition with a molar mass,  $M$ , and a density  $\rho$ :<sup>58</sup>

$$s(t) = \frac{M}{n\rho}N_{\text{SEI}}(t) \quad (13)$$

where  $n$  is the number of Li atoms per SEI component. For the sake of discussion only, the SEI is assumed to be comprised of pure  $\text{Li}_2\text{CO}_3$  ( $M = 29.88 \text{ g mol}^{-1}$ ,  $n = 2$  and  $\rho = 2.01 \text{ g cm}^{-3}$ ); although the presence of organic, less dense components will result in an even thicker SEI than obtained using this composition, the current assumption allows for an order-of-magnitude estimation of the SEI thickness, which is helpful for comparison with experimental data.

## Results

### Constant current deposition in LP30 and LP30 + FEC

Fig. 2a shows the  ${}^7\text{Li}$  *in situ* NMR spectra continuously acquired during a  $0.5 \text{ mA cm}^{-2}$  constant current experiment. The resonance from Li metal depends on the orientation of the Li metal anode strip with respect to the static magnetic field,  $B_0$ , due to Li metal's temperature independent paramagnetism (TIP).<sup>37,44</sup> Aligning the cell perpendicular to the  $B_0$  field results in a  ${}^7\text{Li}$  resonance at around 245 ppm for the pristine Li metal<sup>37</sup> (Fig. 2a) and all *in situ* cells presented in this work were aligned in this fashion. When depositing Li in both LP30 and LP30 + FEC, a new peak around 260 ppm emerges that continues to grow as a current of  $0.5 \text{ mA cm}^{-2}$  is passed (Fig. 2a). This new resonance is indicative of mossy structures growing near to the Li metal surface.<sup>37,39</sup> Whisker-like morphologies are observed in the SEM micrographs as the major morphology after plating for  $3.5 \text{ mA h cm}^{-2}$  in LP30 electrolyte, whereas dense, thick buds (diameter of surface features  $\sim 5\text{--}10 \mu\text{m}$ ) are observed for LP30 + FEC (Fig. 2b).

The overall increase in the  ${}^7\text{Li}$  NMR signal intensity for Li metal can be attributed to the formation of high surface area deposits where the signal intensity is directly proportional to the volume of Li metal excited by the radio-frequency (rf) field.<sup>37,39</sup> The change in the total integrated intensity between 220–280 ppm, termed “total intensity” for the rest of the paper, was converted into the mass change (*i.e.*, the change in the Li mass detected by NMR spectroscopy.),  $\Delta \text{mass}$  (Fig. 2c). The quantification of the NMR signal followed the theory developed





**Fig. 2** (a) *In situ* NMR spectra obtained under a constant current of  $0.5 \text{ mA cm}^{-2}$  in LP30 and LP30 + FEC. (b) SEM images of the microstructures formed on applying a  $0.5 \text{ mA cm}^{-2}$  constant current in LP30 (left) and LP30 + FEC (right). (c) The total integrated intensity detected by NMR converted into mass change (mg) for a constant current of  $0.5 \text{ mA cm}^{-2}$  in LP30 (green) and LP30 + FEC (orange). The dashed line indicates  $m_{\text{echem}}$ , the mass deposited calculated based on the electrochemistry. A total of 6.5C of charge was passed, which corresponds to roughly  $3.5 \text{ mA h cm}^{-2}$ . (d and e) The integrated intensity of the deconvoluted metal peaks and microstructural peak converted into the change in mass,  $\Delta$  mass (mg). (f) An example of how the spectra for the LP30 electrolyte were deconvoluted into two overlapping metal peaks and one microstructural peak.

by Bhattacharyya *et al.* and is described in more detail in the ESI†.<sup>37,39</sup>  $\Delta$  mass is then plotted against charge passed (in C, coulombs) in order to compare it to the total amount of mass of Li deposited based on the electrochemistry,  $m_{\text{echem}} = 0.072 \text{ mg C}^{-1}$  (Fig. 2c). The charge passed in Fig. 2 corresponds roughly to  $3.5 \text{ mA h cm}^{-2}$  (the slight differences between cells arising from small variations in electrode area).  $m_{\text{echem}}$  was calculated by Faraday's law of electrolysis for the ideal case without considering the coulombic losses associated with the formation of the SEI, the competing reaction to Li metal deposition.

For both electrolyte systems, the mass increase calculated from the total intensity is lower than that expected from the applied electrochemistry (Fig. 2c), *i.e.*,  $m_{\text{NMR}} < m_{\text{echem}}$ . There are three possible scenarios that can account for this. In the first scenario, part of the Li is plated as a smooth deposit and does not result in an increased intensity of the Li signal, since it does not change the overall Li metal surface area. This is due to the skin depth effect of metals, where the rf field penetrates only the surface of the metal,  $\sim 12 \mu\text{m}$  for Li, (note that the diamagnetic SEI does not impede rf penetration).<sup>37</sup> In the second scenario, the growth of dense Li metal microstructures may also lead to an attenuation of the rf signal and poor excitation of the underlying bulk film.<sup>38,43</sup> Third, the competing reduction reaction, SEI formation, results in lower Li metal deposition than expected based on the current passed, *i.e.*, lower current efficiency.

To gain more insight into the morphological changes on the electrodes, as well as the causes of  $m_{\text{NMR}} < m_{\text{echem}}$ , we

performed spectral fittings to determine how the relative fractions of the peaks assigned to Li microstructures *vs.* “bulk metal” change upon plating. The spectra were deconvoluted by using two peaks around 245–252.5 ppm (“bulk metal”) and one peak at around 257.5–262.5 ppm corresponding to the microstructural peak (see an example in Fig. 2f and more detailed explanation in the ESI†).<sup>38</sup> We note that previous work has shown both experimentally and with simulations that dendrites and structures growing away from the Li metal surface give rise to larger shift around 270 ppm compared to microstructures close to the surface.<sup>38,39</sup> In the current study, the *in situ* PEEK capsule cell applies constant pressure within the cell and more compact structures form, leading to a narrower range of shifts.<sup>38,60</sup> The observed shifts of the microstructure peaks (Fig. S1†) are thus similar for both electrolytes although the microstructures have very distinct morphologies as seen in the SEM figures (Fig. 2b).<sup>42</sup>

For the LP30 + FEC electrolyte, the initial increase in microstructure intensity is compensated by a concurrent decrease in the metal intensity (Fig. 2d and e, orange, respectively), both corresponding roughly to  $m_{\text{echem}}$  (*i.e.*, the decrease of metal signal is  $-0.07 \text{ mg C}^{-1}$  and increase in microstructural intensity  $0.08 \text{ mg C}^{-1} \sim m_{\text{echem}}$ ) and thus the total signal intensity (total volume of Li detected by NMR) (Fig. 2c, orange) stays almost constant. This is ascribed to an attenuation of the rf field by the thick microstructures formed in LP30 + FEC (Fig. 2b), so that the rf field penetration into the bulk metal is

less than that for the initial Li film. The intensity of the bulk metal peak in the LP30 electrolyte similarly decreases with charge (Fig. 2d, green), but now the steady intensity increase in intensity of the microstructure peak is lower than that observed for LP30 + FEC, corresponding to only  $0.053 \text{ mg C}^{-1}$ , *i.e.*, approximately 74% of what is expected by the electrochemistry. We attribute this to poorer current efficiency as a result of the higher surface area Li whiskers formed in the LP30 electrolyte, as compared to the dense buds formed in LP30 + FEC, coupled with the larger extent of SEI formation on freshly exposed surface.

To explore the effect of current density on both the plating efficiency and the resulting morphology we performed *in situ* NMR at higher constant current densities of 1 and  $2 \text{ mA cm}^{-2}$  (Fig. S24 and S25†). The quantified intensities of the deconvoluted peaks are shown in Fig. 3. For a constant current of  $1 \text{ mA cm}^{-2}$ , the bulk metal peak for LP30 + FEC electrolyte again decreases due to an attenuation of the signal (Fig. 3b, orange), while the increase in the microstructural peak corresponds roughly to  $m_{\text{echem}}$  (Fig. 3c, orange). For the LP30 electrolyte, the bulk metal peak now stays close to constant indicating that more porous structures, growing away from the electrode's surface, are formed; these microstructures no longer shield the bulk metal leaving the intensity detected by the NMR unchanged. Again, the total increase in intensity for LP30 electrolyte is less than  $m_{\text{echem}}$ , indicating that some of the charge is used to form the SEI.

In contrast, for the higher constant current of  $2 \text{ mA cm}^{-2}$ , a close to constant intensity of the metal peak is observed for

both electrolyte systems, with a slight increase occurring after passing 5 coulombs ( $3.25 \text{ mA h cm}^{-2}$ , Fig. 3e). Now  $m_{\text{NMR}}$  is only slightly lower than  $m_{\text{echem}}$  for both electrolytes, indicating a higher current efficiency for the LP30 electrolyte at  $2 \text{ mA cm}^{-2}$ . This is tentatively ascribed to the competing reactions of SEI formation and Li deposition where at higher overpotentials, electrodeposition of Li metal occurs more rapidly than the kinetically-limited degradation reaction involving the electrolyte species.<sup>73</sup> The morphology of the lithium deposits for the two electrodes is now very similar (Fig. S7†).

### Voltage traces in coin cells as an indirect way to study surface kinetics

To study the distinctive SEI formed in the two electrolytes and the corresponding plating behaviour, symmetrical Li–Li coin cells were assembled and cycled using continuous plating and stripping cycles for current densities of 0.5, 1 and  $2 \text{ mA cm}^{-2}$  applied for a total capacity of  $2 \text{ mA h cm}^{-2}$  per cycle (Fig. 4). The full cycling data can be found in the ESI (Fig. S2–S4†). A different protocol was used in the first cycle for the three current densities in order to compare the ‘peaking behaviour’ seen on stripping: while either 0.5, 1 or  $2 \text{ mA cm}^{-2}$  was applied during plating, a current density of  $1 \text{ mA cm}^{-2}$  was used on stripping for the second half of the first cycle (Fig. 4b–d).

The study of the voltage traces follows the methodology introduced in previous studies,<sup>33,74</sup> to observe the characteristic peaking behaviour that originates from pitting of the stripping electrode. Previous reports have assigned the typical voltage profile to specific deposition and pitting processes: when



Fig. 3 The fitted intensities of the *in situ* NMR spectra of Li metal for constant currents of (a–c)  $1 \text{ mA cm}^{-2}$  and (d–f)  $2 \text{ mA cm}^{-2}$  in the two electrolytes LP30 (green) and LP30 + FEC (orange). The dashed line indicates  $m_{\text{echem}}$ , the calculated mass deposited according to the current passed by the electrochemistry.







Fig. 4 Galvanostatic cycling of symmetric Li-coin cells during (a) the first 10 cycles at  $0.5 \text{ mA cm}^{-2}$  for both stripping and plating. In the first cycle, shown in the enlargement in (b),  $0.5 \text{ mA cm}^{-2}$  was used for plating and  $1.0 \text{ mA cm}^{-2}$  for stripping. First cycle using (c)  $1.0$  and (d)  $2.0 \text{ mA cm}^{-2}$  plating and  $1.0 \text{ mA cm}^{-2}$  for stripping. LP30 (green) and LP30 + FEC (orange). The full cycling data for  $1$  and  $2 \text{ mA cm}^{-2}$  can be found in Fig. S3–S4†

plating Li, there is initially a large overpotential associated with the nucleation of Li deposits, which then decreases rapidly towards a local minimum due to an increased surface area for deposition. When switching polarity after the first deposition, the microstructures formed previously in the first half cycle are oxidised and removed from the stripping electrode. When all of the microstructures have been dissolved completely (or been detached from the electrode surface forming ‘dead Li’) the overpotential increases rapidly. A peak is seen as the overpotential drops again, labelled “pitting” in Fig. 4a, as this behaviour has been assigned to the onset of bulk metal dissolution or pitting of the Li metal surface and an increase in surface area.<sup>33,74</sup> When comparing different electrolytes, a more pronounced peaking behaviour has been associated with substantial impedance differences and spatial variations in the SEI layers that lead to non-uniform stripping and the formation of dead Li.<sup>33</sup>

For the first cycle in LP30 a more apparent “pitting” peak is observed that occurs at an earlier time compared to LP30 + FEC (occurring at  $\sim 78\%$  and  $\sim 92\%$  capacity, respectively for  $0.5 \text{ mA cm}^{-2}$ ). Other studies have suggested that this is due to inhomogeneous dissolution of the lithium whiskers that result in dead Li formation and early peaking behaviour. However, the lower plating efficiency quantified with *in situ* NMR can also lead to the early peaking behaviour observed when lower

amounts of microstructures are present. With  $1$  and  $2 \text{ mA cm}^{-2}$ , the peaking in the first cycle (where the stripping current is kept at  $1 \text{ mA cm}^{-2}$ ) occurs at  $85\%$  and  $89\%$  capacity respectively. This correlates well with the *in situ* NMR, which indicated higher plating efficiencies for the higher current densities in LP30. The voltage traces are flatter for the LP30 + FEC electrolyte, as compared to those for LP30, consistent with both the higher plating efficiency seen in the *in situ* NMR and of studies showing minuscule dead lithium formation in LP30 + FEC.<sup>18,35</sup> The lower overpotential observed for LP30 + FEC is somewhat consistent between cells (Fig. S2–S4†), but the overpotential is affected both by the resistances in the cell (in particular of the SEI) and the surface area (which increases during electrodeposition) accounting for variations between cells.

### Pulse plating Li metal

To test the differences in Li deposition between the two electrolytes further, *in situ* NMR measurements using pulsed currents were carried out. When applying a pulsed current, short pulses for a period  $T_{\text{ON}}$  are applied, which is followed by a rest period  $T_{\text{OFF}}$  where no current is passed (schematic, Fig. S5†). During the rest period,  $T_{\text{OFF}}$ , two main processes occur:

(i) Diffusion of Li ions leading to relaxation of concentration gradients in the electrolyte and around protruding points on the



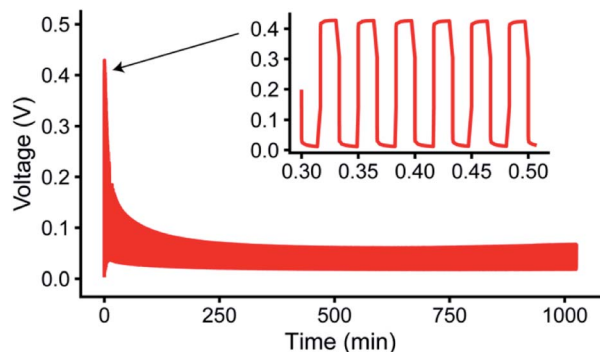


Fig. 5 Representative pulsed current plot for a symmetric Li *in situ* cell at  $1 \text{ mA cm}^{-2}$  with  $T_{\text{ON}}, T_{\text{OFF}} = 1 \text{ s}$  in the LP30 + FEC electrolyte, also shown in Fig. S26.†

electrode, and within the liquid components of the SEI layer; this should result in a more uniform lithium ion distribution near the electrode's surface.<sup>49</sup>

(ii) The chemical formation and growth of the SEI on fresh Li sites (the initial SEI formation has been suggested to be completed in less than 1 s<sup>75,76</sup> but as demonstrated below the full passivation of Li metal can take longer time, up to hours to days). Cracked and newly formed SEI typically has a lower impedance than more mature SEI, which has been suggested to result in preferential deposition sites.<sup>28,33</sup> The formation and

maturation of the SEI during rest periods is likely to increase its impedance and result in levelling effects. As a consequence, Li deposition is anticipated to be more homogeneous using pulse plating. The formation of the SEI during the rest period  $T_{\text{OFF}}$  has also been suggested to increase the current efficiency.<sup>51</sup>

To compare different time scales, both relatively long and short pulse lengths were initially chosen, with  $T_{\text{ON}} = T_{\text{OFF}}$  of either 1 s or 5 ms. The electrochemistry for pulse plating at  $1 \text{ mA cm}^{-2}$  and  $T_{\text{ON}}, T_{\text{OFF}} = 1 \text{ s}$  in LP30 electrolyte is shown in Fig. 5 (see Fig. S26 and S27† for additional pulse plating data for other electrolyte formulations); this corresponds to a duty cycle of  $\theta_{\text{duty}} = T_{\text{ON}}/(T_{\text{ON}} + T_{\text{OFF}}) = 0.5$  and an average current density of  $0.5 \text{ mA cm}^{-2}$ . Thus, the data can be readily compared to the constant current experiments at  $0.5 \text{ mA cm}^{-2}$ .

Fig. 6a shows a comparison of the microstructure masses determined by NMR for both constant plating and pulse plating experiments in LP30. During pulse plating with  $T_{\text{ON}}, T_{\text{OFF}} = 1 \text{ s}$  and  $T_{\text{ON}}, T_{\text{OFF}} = 5 \text{ ms}$  (Fig. 6a), the NMR-derived Li mass changes ( $\Delta \text{mass}$ ) give a slope that corresponds closely to the microstructural mass predicted from the electrochemistry ( $m_{\text{echem}}$ ), indicating high current efficiency of Li metal plating. For both cases, the bulk metal intensity stays close to constant, indicating that the microstructure morphology is more porous as compared to that seen for constant plating at  $0.5 \text{ mA cm}^{-2}$ , and thus does not attenuate the rf field. The resulting morphology (Fig. 6b) for  $T_{\text{ON}}, T_{\text{OFF}} = 1 \text{ s}$ , comprises a mixture of both whisker- and dense-like buds, whereas short pulse lengths,



Fig. 6 Pulse plating in LP30 (a) The deconvoluted intensities of the *in situ* spectra for LP30 during constant plating (CP) at  $0.5 \text{ mA cm}^{-2}$  (green, also plotted in Fig. 2) and pulse plating (PP) at  $1 \text{ mA cm}^{-2}$  with  $T_{\text{ON}}, T_{\text{OFF}} = 1 \text{ s}$  (purple) and  $T_{\text{ON}}, T_{\text{OFF}} = 5 \text{ ms}$  (yellow). The dashed line indicates  $m_{\text{echem}}$ , the mass deposited according to the current passed by the electrochemistry. SEM images of the Li metal morphology using  $1 \text{ mA cm}^{-2}$  and (b)  $T_{\text{ON}}, T_{\text{OFF}} = 1 \text{ s}$  (c)  $T_{\text{ON}}, T_{\text{OFF}} = 5 \text{ ms}$ . (d) The deconvoluted intensities of the *in situ* spectra during pulse plating with  $T_{\text{ON}} : T_{\text{OFF}} = 5 \text{ ms} : 15 \text{ ms}$  using current densities of  $1 \text{ mA cm}^{-2}$  (pink) and  $2 \text{ mA cm}^{-2}$  (blue). SEM images of the Li metal morphology using  $T_{\text{ON}} : T_{\text{OFF}} = 5 \text{ ms} : 15 \text{ ms}$  and (e)  $1 \text{ mA cm}^{-2}$  (f)  $2 \text{ mA cm}^{-2}$ .

$T_{\text{ON}}, T_{\text{OFF}} = 5$  ms, result in the formation of narrow whiskers (Fig. 6c). This demonstrates that applying short pulses in the LP30 electrolyte does not seem to result in more uniform and dense morphologies. To study the effect of the pulse length, we systematically varied the pulse waveforms with  $T_{\text{ON}}, T_{\text{OFF}} = 500$  ms, 100 ms or 50 ms (Fig. S6†) measured with *in situ* NMR spectroscopy. Overall, the slope of the microstructural intensity for all the pulse waveforms is close to  $m_{\text{echem}}$  (Table S2†) indicating higher current efficiency compared to that observed for constant currents. Surprisingly, the most dense microstructures are observed for  $T_{\text{ON}}, T_{\text{OFF}} = 500$  ms and increasingly more open and whisker-like morphologies are seen as the time intervals decrease (Fig. S8†).

To further investigate the effect of the rest period on mitigating microstructural growth, longer rest periods of  $T_{\text{OFF}}$  were explored. Previous studies<sup>50,51,77</sup> have suggested that in order for pulse plating to be beneficial, setting the timings such that  $T_{\text{ON}} < T_{\text{OFF}}$  is crucial, the studies even proposing an optimal  $T_{\text{ON}} : T_{\text{OFF}}$  ratio of close to 1 : 3.<sup>50</sup> Thus, we explored  $T_{\text{ON}} = 5$  ms with a longer rest period  $T_{\text{OFF}} = 15$  ms and  $j_{\text{inst}} = 1$  and 2 mA cm<sup>-2</sup>. This gives average current densities of 0.25 and 0.5 mA cm<sup>-2</sup>. The deconvoluted intensities (Fig. 6d) from the *in situ* NMR measurements show microstructural growth corresponding roughly to  $m_{\text{echem}}$ . Furthermore, the morphology for the lower  $j_{\text{inst}} = 1$  mA cm<sup>-2</sup> remains relatively smooth which can be seen both in the SEM image (Fig. 6e) and with the decreasing metal intensity (Fig. 6d, pink). The attenuation of the bulk

metal signal indicates (for reasons discussed in the previous section) that pulsed currents with  $T_{\text{ON}} < T_{\text{OFF}}$  do indeed lead to more dense deposition near the electrode surface. The SEM images of the plated electrode in Fig. 6e seem to show a significant amount of SEI is present on the Li deposits. To investigate this further and make sure that this was not dried electrolyte, the electrode was transferred back into the glovebox and rinsed with anhydrous DMC. The rinsed electrode (Fig. S10†) was comparable to that in Fig. 6e, indicating that there is significant SEI formed on the Li deposits that is not readily removed by washing.

For the higher current density,  $j_{\text{inst}} = 2$  mA cm<sup>-2</sup>, the morphology again becomes uneven (Fig. 6f), which can also be seen in the intensity of the metal peak (Fig. 6d, blue) that even grows slightly, suggesting roughening on the stripping electrode. Interestingly, we consistently see that the “bulk metal” peak in the *in situ* NMR tends to increase when a relatively high current density is applied, 2 mA cm<sup>-2</sup>, both using constant and pulsed current (Fig. 3e, 6d and 7d). An increase in the bulk metal peak can derive from roughening of the stripping electrode as a result of pitting.<sup>43,78</sup> The effect of pitting on the NMR spectra for LP30, 2 mA cm<sup>-2</sup> and  $T_{\text{ON}} = 5$  ms,  $T_{\text{OFF}} = 15$  ms, was explored by disassembling the *in situ* cell after plating and NMR spectra were taken of the separate electrodes (Fig. S11†). The stripping electrode gives a broader signal, shifted upfield about 2.5 ppm to a value of 247.5 ppm, indicating roughening of the electrode that is consistent with the pits shown in the SEM

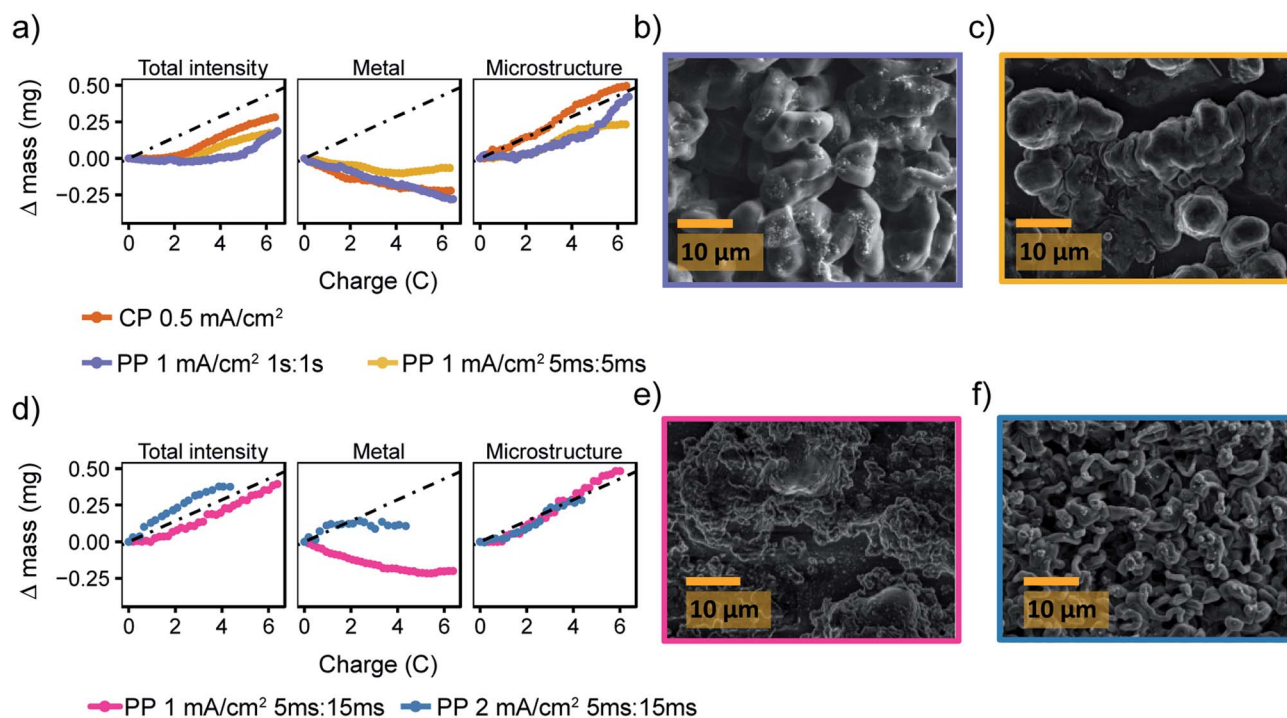


Fig. 7 Pulse plating in LP30 + FEC (a) the deconvoluted intensities of the *in situ* spectra for LP30 + FEC during constant plating (CP) at 0.5 mA cm<sup>-2</sup> (orange, also plotted in Fig. 2) and pulse plating (PP) at 1 mA cm<sup>-2</sup> with  $T_{\text{ON}}, T_{\text{OFF}} = 1$  s (purple) and  $T_{\text{ON}}, T_{\text{OFF}} = 5$  ms (yellow). The dashed line indicates  $m_{\text{echem}}$ , the mass deposited according to the current passed by the electrochemistry. SEM images of the Li metal morphology using 1 mA cm<sup>-2</sup> and (b)  $T_{\text{ON}}, T_{\text{OFF}} = 1$  s (c)  $T_{\text{ON}}, T_{\text{OFF}} = 5$  ms. (d) The deconvoluted intensities of the *in situ* spectra during pulse plating with  $T_{\text{ON}} : T_{\text{OFF}} = 5$  ms : 15 ms using current densities of 1 mA cm<sup>-2</sup> (pink) and 2 mA cm<sup>-2</sup> (blue). SEM images of the Li metal morphology using  $T_{\text{ON}} : T_{\text{OFF}} = 5$  ms : 15 ms and (e) 1 mA cm<sup>-2</sup> (f) 2 mA cm<sup>-2</sup>.



(Fig. S12†).<sup>78</sup> The experiment is not necessarily quantitative as NMR signal intensities depend strongly on the amount of metal inside the NMR coil and considerable errors are introduced when taking the cells in and out of the coil, making it difficult to estimate the extent of pitting on the Li electrode in the current study. Further studies are required to understand the pitting effect where the two Li electrodes can be separated in the coil either in a flooded cell used for MRI studies or with a so-called 'long-design' often used for *in situ* supercapacitor studies to separate the electrodes in the NMR coil.<sup>23,78,79</sup>

The pulse plating experiments were repeated in LP30 + FEC (Fig. 7a) where both long (1 s, purple) and short (5 ms, yellow) pulse lengths seem to delay the onset of the microstructural growth. For both experiments, the microstructural intensity stays constant for the first two coulombs of charge before increasing with a slope close to  $m_{\text{echem}}$ . Thus, we conclude that the  $m_{\text{NMR}} < m_{\text{echem}}$  is a result of smooth deposition that is not detected by the NMR as a result of skin depth effects. The SEM images (Fig. 7b and c) show the resulting relatively smooth and dense morphology of the Li deposits. For  $T_{\text{ON}} : T_{\text{OFF}} = 5 \text{ ms} : 15 \text{ ms}$  and  $j_{\text{inst}} = 1 \text{ mA cm}^{-2}$ , the morphology is even more uniform (Fig. 7e) and for  $j_{\text{inst}} = 2 \text{ mA cm}^{-2}$ , as seen for LP30 (Fig. 6f), the morphology becomes rougher again (Fig. 7d and f).

Overall, pulse plating appears to be more beneficial for Li deposition in the LP30 + FEC electrolyte, which suggests that local concentration gradients at the metal surface are levelled out more effectively. This is not expected to arise from the better transport in the electrolyte as similar  $\text{Li}^+$  diffusion coefficients were measured by PFG-NMR for LP30 with and without an additive ( $D_{\text{LP30}} = 1.70 \times 10^{-10} \text{ m}^2 \text{ s}^{-1}$  and  $D_{\text{LP30+FEC}} = 1.74 \times 10^{-10} \text{ m}^2 \text{ s}^{-1}$ ). That little to no effect is seen on the transport properties on adding FEC is consistent with the molecular dynamics (MD) simulations of Hou *et al.*<sup>80</sup>

### Examining the $\text{Li}^+$ transport properties of the SEI: $^7\text{Li}$ *in situ* NMR measurements of isotope exchange

To understand the effect that the FEC additive has on the SEI formed on Li metal and the corresponding plating behaviour, we performed isotope exchange measurements in both LP30 and LP30 + FEC electrolytes. Using NMR, we observe *in situ* the isotope exchange of  $^6\text{Li}/^7\text{Li}$  ions between  $^6\text{Li}$ -enriched Li metal (95%  $^6\text{Li}$  and 5%  $^7\text{Li}$ ) and natural abundance electrolyte (*i.e.* 92.4%  $^7\text{Li}$  and 7.6%  $^6\text{Li}$ ).<sup>38,58</sup> When  $^6\text{Li}$  metal is soaked in the  $^7\text{Li}$  electrolyte, the exchange between the two isotopes can be described as:



**Fig. 8** (a)  $^7\text{Li}$  NMR spectra of the electrolyte (around 0 ppm) and metal (around 275 ppm) during the  $\sim 75$  hour time period that the  $^6\text{Li}$ -enriched strip of metal was soaked in natural abundance LP30. (b) A schematic showing the dominant processes that determine the exchange rate. (c and d) The intensity changes of the  $^7\text{Li}$  NMR spectra recorded over 75 hours for (c) the lithium metal signal and (d) the diamagnetic lithium signal in the two electrolytes LP30 (green) and LP30 + FEC (orange). The purple curve shows the "control experiment" using a natural abundance Li metal strip where the effect of isotope exchange is removed.





Static  ${}^7\text{Li}$  NMR (Fig. 8a for LP30 electrolyte, Fig. S13b† for LP30 + FEC) was used to follow the changes in signal intensities as a function of time. When the  ${}^6\text{Li}$ -metal is soaked in the  ${}^7\text{Li}$ -electrolyte, the  ${}^7\text{Li}$  NMR signal centred around 0 ppm decreases and the  ${}^7\text{Li}$  metal signal, centred at approximately 275 ppm (the metal is positioned parallel to  $B_0$  field), grows in (Fig. 8a).<sup>44</sup> This is due to the continuous oxidation and reduction between the metal and the electrolyte during equilibrium as described in eqn (1). Because of the skin depth effect, the NMR is only sensitive to the surface layers of the metal whereas the signal intensity for the diamagnetic peak corresponds to the whole volume of the electrolyte and the SEI.

Integration of  ${}^7\text{Li}$  NMR signal intensities as a function of time (Fig. 8c and d) shows significant differences between the two electrolytes; in LP30 + FEC (Fig. 8c, orange) the  ${}^7\text{Li}$  metal intensity increases faster and the  ${}^7\text{Li}$  electrolyte peak intensity drops more quickly compared to LP30 (Fig. 8c and d, green), indicating more rapid exchange of lithium between the metal and electrolyte in the presence of FEC. These trends are shown to be reproducible in Fig. S14.† The processes that can affect the isotope exchange rate are shown in the schematic Fig. 8b. For the metal, the relevant processes are the exchange rate at the surface of the metal and self-diffusion of Li atoms within the metal. In the electrolyte and the SEI, the relevant processes are the desolvation of the  $\text{Li}^+$  ion in the electrolyte, diffusion of  $\text{Li}^+$  in the SEI layer, and the chemical formation of the SEI.

A control experiment, using a natural abundance Li metal electrode ( ${}^7\text{Li}$  rich, 92.4%  ${}^7\text{Li}$  and 7.6%  ${}^6\text{Li}$ ) in LP30 + FEC electrolyte was performed to observe the trends when the effect of isotope exchange is eliminated. The changes in intensities are minimal (Fig. 8c and d, purple) indicating that the formation of the SEI should not change the overall  $\text{Li}^+$  concentration in the electrolyte substantially. The NMR intensity of the electrolyte even increases very slightly (Fig. 8d), which is ascribed to the SEI and partial dissolution of the SEI into the electrolyte.<sup>53</sup>

A mathematical model to describe the  ${}^6\text{Li}/{}^7\text{Li}$  isotopic exchange was developed to extract the associated kinetic data from the NMR experiments, see detailed description in the theory section. Initially, a simplified model was formulated that only takes into account the isotope exchange between the metal and the electrolyte and neglects the formation of the SEI (Model I). The fitting of the experimental curves with Model I and eqn (3)–(7) involves only one fitting parameter,  $J_{\text{ex}}$  and implicitly assumes that the SEI remains constant with time (Fig. 9, dashed lines).  $J_{\text{ex}}$  describes the equilibrium exchange flux of Li between the electrolyte and the metal and includes desolvation of  $\text{Li}^+$  ions, diffusion through the SEI. Values for  $J_{\text{ex}}$  obtained from the least-square fit are  $0.77 \times 10^{-6} \text{ mol m}^{-2} \text{ s}^{-1}$  for LP30 and  $1.5 \times 10^{-6} \text{ mol m}^{-2} \text{ s}^{-1}$  for LP30 + FEC (approximately twice as fast for LP30 + FEC). However, as can be seen in Fig. 9 the experimental curves are not well described by Model I (dashed lines).

The model was then further extended to take into account the long-term formation of the SEI (Model II).<sup>58</sup> To describe the rate of SEI formation the model assumes the formation of the SEI to be proportional to the isotope exchange flux,  $J_{\text{ex}}$  and includes the dimensionless SEI formation constant,  $\alpha_{\text{SEI}}(t)$  (eqn (9)). The rate of SEI formation slows down with time, as can be seen from the impedance analysis in Fig. S20–S22† where the resistance of the SEI formed in LP30 + FEC reaches an equilibrium after approximately 20 hours. This is described with a decreasing exponential (eqn (10)), which includes the fitting parameter  $\beta_{\text{SEI}}$ , the SEI growth constant. In addition, the model includes how the maturation of the SEI leads to reduced permeability and the exchange flux becomes time-dependent,  $J_{\text{ex}}(t)$ , described in eqn (11). The fit to the experimental curves is shown in Fig. 9 (Model II, black lines) and the corresponding parameters are presented in Table 2.

At the beginning of the experiment, the exchange flux for LP30 + FEC,  $J_{\text{ex},0}$  (Table 2), is again roughly two times that for LP30. The ratio between  $J_{\text{ex},0}$  for LP30 + FEC and LP30 is roughly the same for both Model I and Model II (factor of two), although the resulting values of the fitted parameter are different. To examine the sensitivity of the fit to the  $J_{\text{ex},0}$  values and verify the



Fig. 9 The intensity changes of the  ${}^7\text{Li}$  NMR spectra (points) and the model fit results for Model I (dashed lines) and Model II (black lines) for (a) the lithium metal and (b) the lithium ions, in the two electrolytes LP30 (green) and LP30 + FEC (orange).



**Table 2** List of the fitted model parameters ( $J_{\text{ex},0}$ ,  $\beta_{\text{SEI}}$ ,  $\alpha_{\text{SEI},0}$  and  $\beta_{\text{SEI}}$ ) and the derived parameters for the isotopic exchange in the electrolytes, LP30 and LP30 + FEC from Model II

Symbol	Description/unit	LP30	LP30 + FEC	Ratio (LP30 + FEC)/LP30
$J_{\text{ex},0}$	Isotope exchange flux at the time of the first NMR measurement [ $10^{-6} \text{ mol m}^{-2} \text{ s}^{-1}$ ]	1.6	3.1	1.9
$J_{\text{ex},74}$	Isotope exchange flux at 74 h [ $10^{-6} \text{ mol m}^{-2} \text{ s}^{-1}$ ]	0.49	1.2	2.5
$\beta_{\text{ex}}$	SEI permeability constant [ $\text{m}^2 \text{ mol}^{-1}$ ]	19	7.8	0.41
$\alpha_{\text{SEI},0}$	SEI formation proportionality constant dimensionless	0.38	0.85	2.2
$\beta_{\text{SEI}}$	SEI growth constant [ $\text{m}^2 \text{ mol}^{-1}$ ]	8.7	17	2.0
$k_{\text{ex},0}$	Exchange rate constant at time of first NMR measurement [ $10^{-10} \text{ m s}^{-1}$ ]	1.8	3.7	2.1
$k_{\text{SEI},0}$	The SEI formation rate constant [ $10^{-10} \text{ m s}^{-1}$ ]	0.68	3.1	4.6
$k_{\text{SEI},74}$	The SEI formation rate constant at 74 h [ $10^{-10} \text{ m s}^{-1}$ ]	0.13	0.17	1.3
$N_{\text{SEI}}$	Number of moles of SEI formed per surface area at time 74 h [ $\text{mmol m}^{-2}$ ]	61	120	2.0

fit for Model II, the values of  $J_{\text{ex},0}$  were also fixed to the  $J_{\text{ex}}$  values from Model I, reported above. The result, Fig. S19,† shows that we cannot fit the data with the  $J_{\text{ex},0}$  values from Model I. The exchange flux  $J_{\text{ex}}(t)$  is plotted as a function of time in Fig. S17b.† The decrease in the permeability of the SEI due to the growing SEI, captured with  $\beta_{\text{ex}}$ , is greater in LP30, which leads to an increased difference in the effective exchange rate at 74 h, shown in Fig. S17.† The ratio of  $J_{\text{ex},74}$  between the two electrolytes is 2.5 and indicates increasingly reduced transport properties in the LP30-derived SEI.

Multiplying the exchange flux determined at the beginning of the experiment by the Faraday constant gives the isotope exchange current, which results in  $15 \mu\text{A cm}^{-2}$  for LP30 and  $30 \mu\text{A cm}^{-2}$  for LP30 + FEC. The SEI current at OCV is calculated similarly and is around  $6 \mu\text{A cm}^{-2}$  in LP30 and  $26 \mu\text{A cm}^{-2}$  in LP30 + FEC (eqn (9)). Using the Butler-Volmer formalism to describe the exchange current (eqn (2)), we similarly define the isotope exchange current  $j_{\text{ex}}$  and obtain an estimate of  $k_{\text{ex}}$  [ $\text{m s}^{-1}$ ], the isotope exchange rate constant:

$$j_{\text{ex}}(t) = F \times J_{\text{ex}}(t) = Fk_{\text{ex}}(t)[\text{Li}^+]^{\alpha}[\text{Li}^0]^{1-\alpha} \quad (15)$$

The value of the transfer coefficient  $\alpha$ , is assumed to be 0.5, which has been found to fit a range of experimental data adequately<sup>67,81</sup> and the calculated values of  $k_{\text{ex}}$  are listed in Table 2. The SEI formation rate constant can now be defined as  $k_{\text{SEI}} = \alpha_{\text{SEI}}k_{\text{ex}}$  (see eqn (9)). At the start of the experiment,  $k_{\text{SEI}}$  for LP30 + FEC is approximately five times that in LP30 (Table 2). The SEI then reaches equilibrium faster, as seen with higher value of  $\beta_{\text{SEI}}$  (Table 2) and the sharp decrease in  $\alpha_{\text{SEI}}(t)$  shown in Fig. S18.† This is consistent with the impedance acquired in symmetrical Li-Li coin cells at OCV (Fig. S22†) where the impedance in the LP30 + FEC stabilises and plateaus compared to it consistently rising in LP30.

According to the simulation, the number of moles per surface area formed in the two electrolytes,  $N_{\text{SEI}}$  (Fig. S17a†) is also greater for the LP30 + FEC electrolyte, indicating a thicker SEI is being formed. We have estimated the thickness of the SEI by using eqn (13) and assuming it to be pure  $\text{Li}_2\text{CO}_3$  so as to provide a qualitative understanding of the extent of SEI

formation. Averaging over the whole experiment (74 hours) the SEI formation rate is  $6.1 \text{ nm h}^{-1}$  in LP30 and  $12 \text{ nm h}^{-1}$  for LP30 + FEC. The values are relatively large and seem to overestimate the thickness of the SEI but are on a similar scale to what was estimated in an earlier isotope exchange study ( $14 \text{ nm h}^{-1}$  in LP30).<sup>58</sup> One possible reason for this overestimation of thickness is the assumption that all of the reduced electrolyte species are deposited to form the SEI. However, it has been shown experimentally that a wide range of the reduced electrolyte species are soluble and go into the electrolyte.<sup>75,82,83</sup> We also note that the comparison of SEI thicknesses needs to be interpreted with caution as the chemical composition and density is expected to differ between the two electrolytes.

The confidence interval of the fitted parameters is reported in Table S3.† The most important observation from the error analysis is the large interval for  $\beta_{\text{SEI}}$  in LP30, which gives the range  $0\text{--}18 \text{ m}^2 \text{ mol}^{-1}$ , whereas the confidence interval for LP30 + FEC is  $11\text{--}23 \text{ m}^2 \text{ mol}^{-1}$ . This may indicate that the exponential decay of the SEI growth rate with time (eqn (10)) does not fully capture the SEI formation process in LP30. Alternatively, and more plausibly, this could also demonstrate the instability of the SEI formed in LP30 which has been shown to form more soluble SEI products in studies on silicon compared to LP30 + FEC.<sup>84</sup> This explanation is consistent with the impedance data (Fig. S20†), where the resistance of the SEI for LP30,  $R_{\text{SEI}}$ , keeps growing with time.

## Discussion

Localised deposition has previously been associated with slow  $\text{Li}^+$  transport properties in the SEI, which leads to induced stresses beneath the SEI and can cause fracture, resulting in Li whisker growth.<sup>28,30,85</sup> The numerical simulations of the isotope exchange curves show that the  $\text{Li}^+\text{--Li}^0$  exchange rate, quantified here *via* the isotope exchange flux  $J_{\text{ex}}$ , through the LP30 + FEC chemically-derived SEI is twice as fast as transport through the LP30-derived SEI (Table 2) and the more whisker-like morphology that forms in LP30 can, at least in part, be explained by the slower  $\text{Li}^+$  transport in the SEI. Furthermore, rapid passivation on fresh Li metal surfaces has been argued to



be a key parameter of a good SEI layer.<sup>86</sup> If the SEI breaks, fast SEI repair will reduce the impedance differences on different sites on the electrode's surface resulting in more homogeneous deposition.<sup>33</sup> The simulations of the isotope exchange indicate that the SEI growth rate is more than four times faster in LP30 + FEC, clearly demonstrating the faster kinetics associated with FEC degradation. This is consistent with the higher reduction potential of FEC<sup>80</sup> that has been shown to occur at  $\sim 1.3$  V compared to  $\sim 0.8$  V (vs. Li/Li<sup>+</sup>) for the EC solvent molecule.<sup>87</sup> NMR studies (albeit on silicon anodes<sup>88,89</sup>) have also shown that the organic polymers within the SEI formed with FEC additives contain more cross-linking groups, consistent with a more elastic and flexible SEI, that can accommodate to a greater extent the growth of Li deposits without cracking or rupturing.

Our results from the isotope exchange simulations should be contrasted with those of Boyle *et al.* who measured the exchange current density for Li metal deposition (using an ultramicroelectrode and fast scan rates of  $>1000$  mV s<sup>-1</sup> to minimise SEI effects) and found that  $j_0$  was approximately 1.5 times larger for a carbonate electrolyte with vs. without FEC.<sup>67</sup> They attributed the faster electron transfer kinetics to the slightly lower Li<sup>+</sup> concentration when the FEC is added to the electrolyte and thus weaker interactions between ions.<sup>67</sup> In our study, the exchange is measured at OCV and depends on both the electron kinetics and the mass transport through the SEI. This latter point is evident in the simulations where  $J_{\text{ex}}$  was found to be time-dependent because of the growing SEI, the exchange flux decreasing over the whole time period (Fig. S17†). We further note that the exchange current estimated by isotope exchange is three orders of magnitude lower than that obtained by Boyle *et al.* by Li plating on a tungsten-ultramicroelectrode (with little to no SEI) and an order of magnitude lower than that estimated by impedance spectroscopy (with SEI).<sup>67</sup> This is partly because the NMR measurements are not started until approximately 10 minutes after the Li metal is immersed in the electrolyte. The numbers extracted from our measurements are particularly relevant to the corrosion seen for Li metal anodes<sup>90,91</sup> (particularly when high surface area mossy and dendritic structures are formed) and also for Li formed on graphitic anodes under high currents/low temperatures.

Our results suggest that the lower coulombic efficiencies frequently reported for the commercial carbonate electrolyte<sup>15</sup> are due to both low current efficiency with continuous SEI formation as a result of the formation of higher surface area Li whiskers and the formation of dead lithium (in cycling experiments). The former is demonstrated by using *in situ* NMR, where the mass of the Li deposits can be quantified and readily compared to the mass expected to be deposited from the electrochemistry,  $m_{\text{echem}}$  (Table S1†). This is also consistent with the earlier "peaking" behaviour seen for the LP30 electrolyte during the 1<sup>st</sup> stripping (Fig. 4). For the faster plating current density of 2 mA cm<sup>-2</sup>, the current efficiency (Fig. 3) and the morphology of the Li deposits become similar for the two electrolytes (see SEM, Fig. S7,† consistent with other studies<sup>18</sup>). This demonstrates that although the SEI in LP30 + FEC has better transport properties, at high current densities it is still not fast enough to allow for a sufficiently uniform transport through the SEI. We note that there may be differences between the chemically formed SEI studied with the isotope exchange and

that formed on cycling in terms of composition and morphology. Further experiments are in progress to explore this in more detail using dynamic nuclear polarization (DNP) NMR.<sup>92</sup>

The SEI formed during the rest period in pulse plating is directly related to the isotope exchange measurements, as it forms under OCV. For the pulse plating experiments, the morphology of the Li deposits in LP30 were seen to be highly dependent on both plating and rest time. Previous Monte Carlo simulations have suggested shorter pulses are beneficial in mitigating Li dendrite growth.<sup>77</sup> In our experiments in LP30, the longer pulses of both  $T_{\text{ON}}$ ,  $T_{\text{OFF}} = 1$  s and 500 ms resulted in a denser morphology than achieved on constant plating whereas  $T_{\text{ON}}$ ,  $T_{\text{OFF}} = 5$  ms resulted in the formation of narrow whiskers. Therefore, recommending short pulses for Li deposition, nominally to ensure minimal concentration gradients at the electrode's surface, may not always be appropriate. The results illustrate the important effect of the rest period in pulse plating Li metal, where both diffusion and the healing of the SEI layer takes place. Applying a longer rest time for the short pulses, using  $T_{\text{ON}} = 5$  ms and  $T_{\text{OFF}} = 15$  ms, improved the plating with smoother deposits forming (Fig. 5e). Of note, as shown both with the impedance measurements (Fig. S22†) and the isotope exchange simulations, full passivation of the Li metal surface is not achieved on the timescale of the rest periods used in the pulse plating experiments. Despite this, all *in situ* pulse plating experiments demonstrated that less charge was wasted to form the SEI during plating and indicates that even time intervals of 15 ms can be sufficient to at least partially heal hotspots formed during plating. Note that this process still consumes lithium (and electrolyte) (*via* reactions such as those described in eqn (8)) and hence is another mechanism responsible for degradation in a metal cell: in experiments performed with a fixed and finite lithium concentration (*e.g.*, when plating using a lithium-ion cathode as the lithium source), this will lead to more rapid cell death.

Pulse plating in LP30 + FEC led consistently to more dense morphologies and was seen to delay the onset of microstructural formation (Fig. 6a). There are three possible explanations for pulse plating being more effective in LP30 + FEC. As we have shown in the first section, the microstructures formed under constant plating in LP30 + FEC are generally more uniform compared to LP30. Hence, local concentration gradients that develop at the electrode during plating, which are amplified at rough sites and protrusions, are less pronounced for the smoother metal surface in LP30 + FEC. Thus, (i) relaxation of local concentration gradients will not be as important as in the case for LP30. (ii) Based on our simulations, SEI passivation will occur more rapidly, reducing impedance differences over the electrode's surface. (iii) The SEI in LP30 + FEC allows for more rapid Li<sup>+</sup> transport than in LP30, demonstrated by the Li<sup>+</sup> exchange rate, and thus more homogeneous plating is expected.

## Conclusion

Overall, this work has presented a careful comparison of the SEI formed in the standard carbonate electrolyte, LP30, and in LP30 + FEC with quantitative and non-invasive NMR measurements.



Our *in situ* NMR measurements have shown that both the plating efficiency and growth mode of lithium deposition are governed by the nature of the SEI as well as the applied current density. Pulse plating was shown to be more effective in LP30 + FEC, delaying the onset of microstructural growth.

Using  $^6\text{Li}/^7\text{Li}$  isotope exchange NMR measurements,  $\text{Li}^+$  exchange between Li metal and the electrolyte was studied (at OCV), the exchange occurring simultaneously with SEI growth. The measured exchange flux was related to the traditional Butler–Volmer model of electrochemical kinetics. Measuring the  $^6\text{Li}/^7\text{Li}$  isotope exchange is shown to be an easy and effective method to monitor the exchange current (affected by transport through the SEI) and the growth of SEI on lithium metal anodes. The exchange current is shown to decrease with time, corresponding to a decreased permeability of the SEI. By performing numerical simulations, we demonstrate that the method can be used to compare the exchange rates at equilibrium (OCV) and the kinetics of SEI formation on Li metal, for a range of different electrolytes and electrolyte additives. The values obtained are highly relevant for understanding why pulse plating can lead to smoother deposition, and allow Li corrosion to be directly quantified.

The two electrolytes studied in this work show clear differences: the  $^6\text{Li}/^7\text{Li}$  exchange is twice as fast in LP30 + FEC (due to faster  $\text{Li}^+$  transport in the SEI), and the SEI formation rate is more than four times faster, as compared to LP30. For LP30, the slower  $\text{Li}^+$  transport can lead to non-uniform current distribution during plating, localised deposition resulting in stress-build up in the SEI and whisker-growth. The high surface area of the whiskers leads to low current efficiency due to constant SEI formation, the slow SEI formation rate also impeding the full repair of the SEI.

*Via* this NMR study we identify and quantify some of the key SEI parameters – namely the lithium ion transport and the rate of healing – that are important in controlling the nature of lithium metal deposition. Future studies with a much wider range of additives and electrolytes are in progress to use this methodology to help design an optimal SEI layer on lithium metal that achieves uniform plating and stripping at commercially relevant current densities ( $>0.5 \text{ mA cm}^{-2}$ ) with high coulombic efficiencies.

## Data availability

The raw intensity data from the isotope exchange measurements, the raw EIS data and the Matlab codes to run the simulations according to the mathematical model presented in the current study are available in the Apollo University of Cambridge repository at <https://doi.org/10.107863/CAM.54707>

## Conflicts of interest

There are no conflicts to declare.

## Acknowledgements

A. B. G and S. V acknowledge the support from the Royal Society (RP/R1/180147). A. B. G also acknowledges EPSRC-EP/M009521/1

for funding and S. V. acknowledges the Faraday Institution (SOL-BAT, FIRG007) and Cambridge Trust for funding. S. M thanks the Blavatnik Cambridge Fellowships. L. E. M. gratefully acknowledges financial support through a H2020 Marie Skłodowska-Curie Individual Fellowship and a Charles and Katharine Darwin Research Fellowship (Darwin College). C. P. G thanks the EU/ERC for an Advanced Fellowship (Grant Agreement No. 835073). A. B. G thanks the NanoDTC Cambridge for travel funding. We would like to thank Dr Adam Best (CSIRO) and Dr Amangeldi Torayev (University of Oxford) for useful discussions. Finally, we would like to thank Sharon Connor for careful reading of the manuscript and one of the reviewers for their helpful comments concerning the exchange model.

## References

- 1 P. G. Bruce, S. A. Freunberger, L. J. Hardwick and J.-M. Tarascon, *Nat. Mater.*, 2012, **11**, 172.
- 2 W. Xu, J. Wang, F. Ding, X. Chen, E. Nasybulin, Y. Zhang and J.-G. G. Zhang, *Energy Environ. Sci.*, 2014, **7**, 513–537.
- 3 K. N. Wood, M. Noked and N. P. Dasgupta, *ACS Energy Lett.*, 2017, **2**, 664–672.
- 4 B. Liu, J.-G. G. Zhang and W. Xu, *Joule*, 2018, **2**, 833–845.
- 5 M. Paunovic and M. Schlesinger, *Fundamentals of Electrochemical Deposition*, John Wiley & Sons, Inc., Hoboken, NJ, USA, 2006.
- 6 Y. S. Cohen, Y. Cohen and D. Aurbach, *J. Phys. Chem. B*, 2000, **104**, 12282–12291.
- 7 S. Jurng, Z. L. Brown, J. Kim and B. L. Lucht, *Energy Environ. Sci.*, 2018, **11**, 2600–2608.
- 8 X. Q. Zhang, X. Chen, X. B. Cheng, B. Q. Li, X. Shen, C. Yan, J. Q. Huang and Q. Zhang, *Angew. Chem., Int. Ed.*, 2018, **100081**, 5301–5305.
- 9 J. Qian, W. Xu, P. Bhattacharya, M. Engelhard, W. A. Henderson, Y. Zhang and J. G. Zhang, *Nano Energy*, 2015, **15**, 135–144.
- 10 J. Zheng, M. H. Engelhard, D. Mei, S. Jiao, B. J. Polzin, J. G. Zhang and W. Xu, *Nat. Energy*, 2017, **2**, 1–15.
- 11 E. Markevich, G. Salitra, F. Chesneau, M. Schmidt and D. Aurbach, *ACS Energy Lett.*, 2017, **2**, 1321–1326.
- 12 R. Mogi, M. Inaba, Y. Iriyama, T. Abe and Z. Ogumi, *J. Electrochem. Soc.*, 2002, **149**, A385.
- 13 J. Heine, P. Hilbig, X. Qi, P. Niehoff, M. Winter and P. Bieker, *J. Electrochem. Soc.*, 2015, **162**, A1094–A1101.
- 14 F. Ding, W. Xu, X. Chen, J. Zhang, M. H. Engelhard, Y. Zhang, B. R. Johnson, J. V. Crum, T. A. Blake, X. Liu and J.-G. Zhang, *J. Electrochem. Soc.*, 2013, **160**, A1894–A1901.
- 15 X. Q. Zhang, X. B. Cheng, X. Chen, C. Yan and Q. Zhang, *Adv. Funct. Mater.*, 2017, **27**, 1–8.
- 16 Z. L. Brown, S. Jurng, C. C. Nguyen and B. L. Lucht, *ACS Appl. Energy Mater.*, 2018, **1**, 3057–3062.
- 17 Y. Li, Y. Li, A. Pei, K. Yan, Y. Sun, C. L. Wu, L. M. Joubert, R. Chin, A. L. Koh, Y. Yu, J. Perrino, B. Butz, S. Chu and Y. Cui, *Science*, 2017, **358**, 506–510.
- 18 Y. Li, W. Huang, Y. Li, A. Pei, D. T. Boyle and Y. Cui, *Joule*, 2018, **2**, 2167–2177.





- 19 J. L. Barton and J. O. Bockris, *Proc. R. Soc. A*, 1962, **268**, 485–505.
- 20 J. N. Chazalviel, *Phys. Rev. A*, 1990, **42**, 7355–7367.
- 21 H. J. S. Sand, *London, Edinburgh, Philos. Mag.*, 1901, **1**, 45–79.
- 22 C. Brissot, M. Rosso, J. N. Chazalviel and S. Lascaud, *J. Power Sources*, 1999, **81**, 925–929.
- 23 H. J. Chang, A. J. Iltott, N. M. Trease, M. Mohammadi, A. Jerschow and C. P. Grey, *J. Am. Chem. Soc.*, 2015, **137**, 15209–15216.
- 24 P. Bai, J. Li, F. R. Brushett and M. Z. Bazant, *Energy Environ. Sci.*, 2016, **9**, 3221–3229.
- 25 K. Nishikawa, T. Mori, T. Nishida, Y. Fukunaka and M. Rosso, *J. Electroanal. Chem.*, 2011, **661**, 84–89.
- 26 G. Yoon, S. Moon, G. Ceder and K. Kang, *Chem. Mater.*, 2018, **30**, 6769–6776.
- 27 K. Nishikawa, T. Mori, T. Nishida, Y. Fukunaka, M. Rosso and T. Homma, *J. Electrochem. Soc.*, 2010, **157**, A1212.
- 28 A. Kushima, K. P. So, C. Su, P. Bai, N. Kuriyama, T. Maebashi, Y. Fujiwara, M. Z. Bazant and J. Li, *Nano Energy*, 2017, **32**, 271–279.
- 29 O. Crowther and A. C. West, *J. Electrochem. Soc.*, 2008, **155**, A806.
- 30 J. Yamaki, S. Tobishima, K. Hayashi, K. Saito, Y. Nemoto and M. Arakawa, *J. Power Sources*, 1998, **74**, 219–227.
- 31 H. Yang, E. O. Fey, B. D. Trimm, N. Dimitrov and M. S. Whittingham, *J. Power Sources*, 2014, **272**, 900–908.
- 32 J. Steiger, D. Kramer and R. Mönig, *Electrochim. Acta*, 2014, **136**, 529–536.
- 33 K. N. Wood, E. Kazyak, A. F. Chadwick, K. H. Chen, J. G. Zhang, K. Thornton and N. P. Dasgupta, *ACS Cent. Sci.*, 2016, **2**, 790–801.
- 34 X. Wang, M. Zhang, J. Alvarado, S. Wang, M. Sina, B. Lu, J. Bouwer, W. Xu, J. Xiao, J. G. Zhang, J. Liu and Y. S. Meng, *Nano Lett.*, 2017, **17**, 7606–7612.
- 35 C. Fang, J. Li, M. Zhang, Y. Zhang, F. Yang, J. Z. Lee, M.-H. Lee, J. Alvarado, M. A. Schroeder, Y. Yang, B. Lu, N. Williams, M. Ceja, L. Yang, M. Cai, J. Gu, K. Xu, X. Wang and Y. S. Meng, *Nature*, 2019, **572**, 511–515.
- 36 J. Wandt, C. Marino, H. A. Gasteiger, P. Jakes, R. A. Eichel and J. Granwehr, *Energy Environ. Sci.*, 2015, **8**, 1358–1367.
- 37 R. Bhattacharyya, B. Key, H. Chen, A. S. Best, A. F. Hollenkamp and C. P. Grey, *Nat. Mater.*, 2010, **9**, 504–510.
- 38 H. J. Chang, N. M. Trease, A. J. Iltott, D. Zeng, L. S. Du, A. Jerschow and C. P. Grey, *J. Phys. Chem. C*, 2015, **119**, 16443–16451.
- 39 S. Chandrashekar, N. M. Trease, H. J. Chang, L.-S. S. Du, C. P. Grey and A. Jerschow, *Nat. Mater.*, 2012, **11**, 311–315.
- 40 A. J. Iltott, M. Mohammadi, H. J. Chang, C. P. Grey and A. Jerschow, *Proc. Natl. Acad. Sci. U. S. A.*, 2016, **113**, 10779–10784.
- 41 P. M. Bayley, N. M. Trease and C. P. Grey, *J. Am. Chem. Soc.*, 2016, **138**, 1955–1961.
- 42 V. Küpers, M. Kolek, P. Bieker, M. Winter and G. Brunklaus, *Phys. Chem. Chem. Phys.*, 2019, **21**, 26084–26094.
- 43 H. Wang, N. Sa, M. He, X. Liang, L. F. Nazar, M. Balasubramanian, K. G. Gallagher and B. Key, *J. Phys. Chem. C*, 2017, **121**, 6011–6017.
- 44 N. M. Trease, L. Zhou, H. J. Chang, B. Y. Zhu and C. P. Grey, *Solid State Nucl. Magn. Reson.*, 2012, **42**, 62–70.
- 45 H. Y. Cheh, *J. Electrochem. Soc.*, 1971, **118**, 551–557.
- 46 Y. Fukunaka, *J. Electrochem. Soc.*, 1989, **136**, 3278.
- 47 A. Ul-Hamid, H. Dafalla, A. Quddus, H. Saricimen and L. M. Al-Hadhrani, *Appl. Surf. Sci.*, 2011, **257**, 9251–9259.
- 48 K. I. Popov, M. D. Maksimović, B. M. Ocololjić and B. J. Lazarević, *Surf. Technol.*, 1980, **11**, 99–109.
- 49 N. Ibl, *Surf. Technol.*, 1980, **10**, 81–104.
- 50 Q. Li, S. Tan, L. Li, Y. Lu and Y. He, *Sci. Adv.*, 2017, **3**, 1–10.
- 51 A. Maraschky and R. Akolkar, *J. Electrochem. Soc.*, 2018, **165**, D696–D703.
- 52 G. García, S. Dieckhöfer, W. Schuhmann and E. Ventosa, *J. Mater. Chem. A*, 2018, **6**, 4746–4751.
- 53 D. Rehnlund, C. Ihrfors, J. Maibach and L. Nyholm, *Mater. Today*, 2018, **21**, 1010–1018.
- 54 G. E. Boyd, A. W. Adamson and L. S. Myers, *J. Am. Chem. Soc.*, 1947, **69**, 2836–2848.
- 55 F. G. Helfferich, in *Mass Transfer and Kinetics of Ion Exchange*, 1983.
- 56 M. Kosmulski, M. Jaroniec and J. Szczypta, *Adsorpt. Sci. Technol.*, 1985, **2**, 97–119.
- 57 T.-C. Huang and F.-N. Tsai, *J. Chem. Eng. Jpn.*, 1977, **10**, 131–136.
- 58 A. J. Iltott and A. Jerschow, *J. Phys. Chem. C*, 2018, **122**, 12598–12604.
- 59 A. J. Bard and L. R. Faulkner, *Electrochemical Methods Fundamentals of Electrochemistry*, 2001.
- 60 O. Pecher, J. Carretero-Gonzalez, K. J. J. Griffith and C. P. P. Grey, *Chem. Mater.*, 2017, **29**, 213–242.
- 61 J. M. Stratford, P. K. Allan, O. Pecher, P. A. Chater and C. P. Grey, *Chem. Commun.*, 2016, **52**, 12430–12433.
- 62 H. Wickham, R. Francois, L. Henry and K. Müller, *Cran*, 2017.
- 63 A. J. Iltott, S. Chandrashekar, A. Klöckner, H. J. Chang, N. M. Trease, C. P. Grey, L. Greengard and A. Jerschow, *J. Magn. Reson.*, 2014, **245**, 143–149.
- 64 E. O. Stejskal and J. E. Tanner, *J. Chem. Phys.*, 1965, **42**, 288–292.
- 65 K. Zick, *Diffusion NMR User Manual*, Bruker Corporation, 2016.
- 66 P. Atkins, J. de Paula and J. Keeler, *Atkins' Physical Chemistry*, Oxford University Press, Oxford, United Kingdom, 2018.
- 67 W. Huang, D. T. Boyle, Y. Li, Y. Li, A. Pei, H. Chen and Y. Cui, *ACS Nano*, 2019, **13**, 737–744.
- 68 R. Messer and F. Noack, *Appl. Phys.*, 1975, **6**, 79–88.
- 69 D. Aurbach, *J. Power Sources*, 2000, **89**, 206–218.
- 70 J. Christensen and J. Newman, *J. Electrochem. Soc.*, 2004, **151**, A1977.
- 71 M. Tang and J. Newman, *J. Electrochem. Soc.*, 2012, **159**, A1922–A1927.
- 72 L. F. Shampine and M. W. Reichelt, *J. Sci. Comput.*, 1995, **18**, 1–22.
- 73 D. Aurbach and M. Moshkovich, *J. Electrochem. Soc.*, 1998, **145**, 2629.
- 74 G. Bieker, M. Winter and P. Bieker, *Phys. Chem. Chem. Phys.*, 2015, **17**, 8670–8679.



- 75 D. Aurbach and A. Zaban, *J. Electroanal. Chem.*, 1994, **367**, 15–25.
- 76 M. Odziemkowski, *J. Electrochem. Soc.*, 1993, **140**, 1546.
- 77 A. Aryanfar, D. Brooks, B. V. Merinov, W. A. Goddard, A. J. Colussi and M. R. Hoffmann, *J. Phys. Chem. Lett.*, 2014, **5**, 1721–1726.
- 78 L. E. Marbella, S. Zekoll, J. Kasemchainan, S. P. Emge, P. G. Bruce and C. P. Grey, *Chem. Mater.*, 2019, **31**, 2762–2769.
- 79 H. Wang, T. K. J. Köster, N. M. Trease, J. Ségalini, P. L. Taberna, P. Simon, Y. Gogotsi and C. P. Grey, *J. Am. Chem. Soc.*, 2011, **133**, 19270–19273.
- 80 T. Hou, G. Yang, N. N. Rajput, J. Self, S.-W. Park, J. Nanda and K. Persson, *Nano Energy*, 2019, **64**, 103881.
- 81 M. W. Verbrugge and B. J. Koch, *J. Electrochem. Soc.*, 1994, **141**, 3053.
- 82 K. Tasaki, A. Goldberg, J.-J. Lian, M. Walker, A. Timmons and S. J. Harris, *J. Electrochem. Soc.*, 2009, **156**, A1019.
- 83 M. Tang, S. Lu and J. Newman, *J. Electrochem. Soc.*, 2012, **159**, A1775–A1785.
- 84 Y. Jin, N. J. H. Kneusels, P. C. M. M. Magusin, G. Kim, E. Castillo-Martínez, L. E. Marbella, R. N. Kerber, D. J. Howe, S. Paul, T. Liu and C. P. Grey, *J. Am. Chem. Soc.*, 2017, **139**, 14992–15004.
- 85 Y. He, X. Ren, Y. Xu, M. H. Engelhard, X. Li, J. Xiao, J. Liu, J. G. Zhang, W. Xu and C. Wang, *Nat. Nanotechnol.*, 2019, **14**, 1042–1047.
- 86 M. He, R. Guo, G. M. Hobold, H. Gao and B. M. Gallant, *Proc. Natl. Acad. Sci. U. S. A.*, 2020, **117**, 73–79.
- 87 C. Xu, F. Lindgren, B. Philippe, M. Gorgoi, F. Björefors, K. Edström and T. Gustafsson, *Chem. Mater.*, 2015, **27**, 2591–2599.
- 88 Y. Jin, N. J. H. Kneusels, L. E. Marbella, E. Castillo-Martínez, P. C. M. M. Magusin, R. S. Weatherup, E. Jónsson, T. Liu, S. Paul and C. P. Grey, *J. Am. Chem. Soc.*, 2018, **140**, 9854–9867.
- 89 A. L. Michan, M. Leskes and C. P. Grey, *Chem. Mater.*, 2016, **28**, 385–398.
- 90 D. Lin, Y. Liu, Y. Y. Li, Y. Y. Li, A. Pei, J. Xie, W. Huang and Y. Cui, *Nat. Chem.*, 2019, **11**, 382–389.
- 91 A. Kolesnikov, M. Kolek, J. F. Dohmann, F. Horsthemke, M. Börner, P. Bieker, M. Winter and M. C. Stan, *Adv. Energy Mater.*, 2020, **2000017**, 1–9.
- 92 M. A. Hope, B. L. D. Rinkel, A. B. Gunnarsdóttir, K. Märker, S. Menkin, S. Paul, I. V. Sergeev and C. P. Grey, *Nat. Commun.*, 2020, **11**, 2224.

